



Enhancing Coupling Resonance in Multilayer MIM Structure and F-P Cavity Mode for Mid-Infrared Band Applications

Zhihui Wei^{1,2} · Hai Liu¹ · Bo Wang^{1,2} · Jian Zhang¹ · Haolong Tang¹ · Qiang Li¹ · Zhenfeng Shen¹ · Haigui Yang¹ · Dongzhi Shan¹ · Yuanhang Zhao^{1,2} · Yi Zhao¹ · Kai Wang^{1,2} · Xiaoyi Wang¹

Received: 9 November 2023 / Accepted: 12 December 2023
© The Author(s), under exclusive licence to Springer Science+Business Media, LLC, part of Springer Nature 2023

Abstract

In this paper, we propose a cavity-coupled perfect absorber (CCPA) consisting of a bottom gold layer, a SiO₂ layer, and multilayer MIM (metal–insulator–metal) nanowires. By coupling the Fabry–Pérot (F-P) cavity mode with the magnetic plasmons (MPs) resonance mode in multilayer MIM structure, the MPs resonance in the multilayer MIM structure is enhanced and leads to increased absorption of the structure. By designing and optimizing the parameters, near-perfect absorption in the mid-infrared wavelengths can be achieved. The positions of the two absorption peaks can be adjusted by changing the width of the nanowires and the thickness of the SiO₂ layer, resulting in the formant excitation at any position in the mid-infrared. The full-width at half-maximum (FWHM) of the short-wave peak is only 0.076 μm, and the FWHM of the long-wave peak is only 0.46 μm. The long-wave absorption peak maintains high efficiency and stability even at large incident angles, exhibiting “omnidirectional” characteristics. The tunable mid-infrared emission peak can be matched to the characteristic spectra of gases, making it suitable for infrared radiation sources in gas detection.

Keywords Metal-Insulator-Metal · Magnetic plasmons (MPs) resonance · Surface plasmon polariton

Introduction

The metasurface structure can change the amplitude, phase, polarization, and coherence of incident light by designing and optimizing the size, material, and shape of structural units, thereby achieving artificial regulation of spectral response [1]. The use of metasurface structures can achieve optical properties such as negative refractive index [2, 3], negative reflection [4], zero refractive index [5], and metalens [6, 7]. Compared with most traditional optical components, the ultra-strong control level of incident light in metasurface structures allows them to be designed to perform various optical functions. Moreover, metasurface structures have the advantages of small size and lightweight, making them an ideal choice to replace many traditional optical devices. These excellent optical properties have played a driving role in the development

of applications such as electromagnetic stealth [8], super-resolution optical imaging [9], and solar cells [10].

Perfect absorbers have great application value in many fields, including sensors [11, 12], energy harvesting [13–15], thermal radiation [16], and photodetectors [17]. Metal–insulator–metal (MIM) is one of the most common structural units that make up metasurfaces. The plasmonic effect in the subwavelength gap between two metallic regions can significantly enhance the electric and magnetic fields [18–20]. Exciting magnetic plasmons (MPs) resonance through MIM structure can also exhibit absorption characteristics of light [21]. In recent years, many researchers have conducted relevant reports and studies. For example, in 2015, Tittel et al. utilized GST as a dielectric layer for MIM to achieve nearly 90% absorptance in the mid-infrared band [22]. In 2018, Liu et al. proposed a mid-infrared grating-structured metamaterial absorber based on multilayer MIM, but the absorptance was not high, only 80% [23]. In addition, MIM structures with multiple resonance mode effects also have great research value in the optical sensing domain [24–26]. For MIM structural units, in addition to MPs resonance, when the thickness of the dielectric layer increases to a certain parameter, a longitudinal F-P cavity mode will be formed [27], which means that the absorption ability in the

✉ Hai Liu
nmliuhai@163.com

¹ Key Laboratory of Optical System Advanced Manufacturing Technology, Fine Mechanics and Physics, Changchun Institute of Optics, Chinese Academy of Sciences, Changchun 130033, China

² University of the Chinese Academy of Sciences, Beijing 100039, China

mid-infrared band can be further improved through coupling between modes. This will provide guidance for the design and application of relevant metasurface absorbers.

In this paper, we design and fabricate a TM-polarized light dual-band absorber based on a 7-layer MIM structure coupled with an F-P cavity. By optimizing the structural parameters, two absorption peaks with high absorptance are obtained in the mid-infrared band. As the length of the F-P cavity increases, coupling occurs between F-P cavity resonance and MPs, and different cavity lengths directly affect the degree of coupling. By selecting the appropriate cavity length, near-perfect absorption characteristics of mid-infrared can be achieved. At the

same time, it can maintain a highly stable absorption peak under high-angle incidence. Through finite difference time domain (FDTD) electromagnetic modeling and system experiments, we quantitatively captured the impact of the coupling of two modes on the overall absorption of the system.

Simulation and Modeling

Figure 1a is a schematic diagram of the cavity coupling perfect absorber (CCPA) structure composed of a multilayer MIM structure and an F-P cavity. The structure consists of a gold

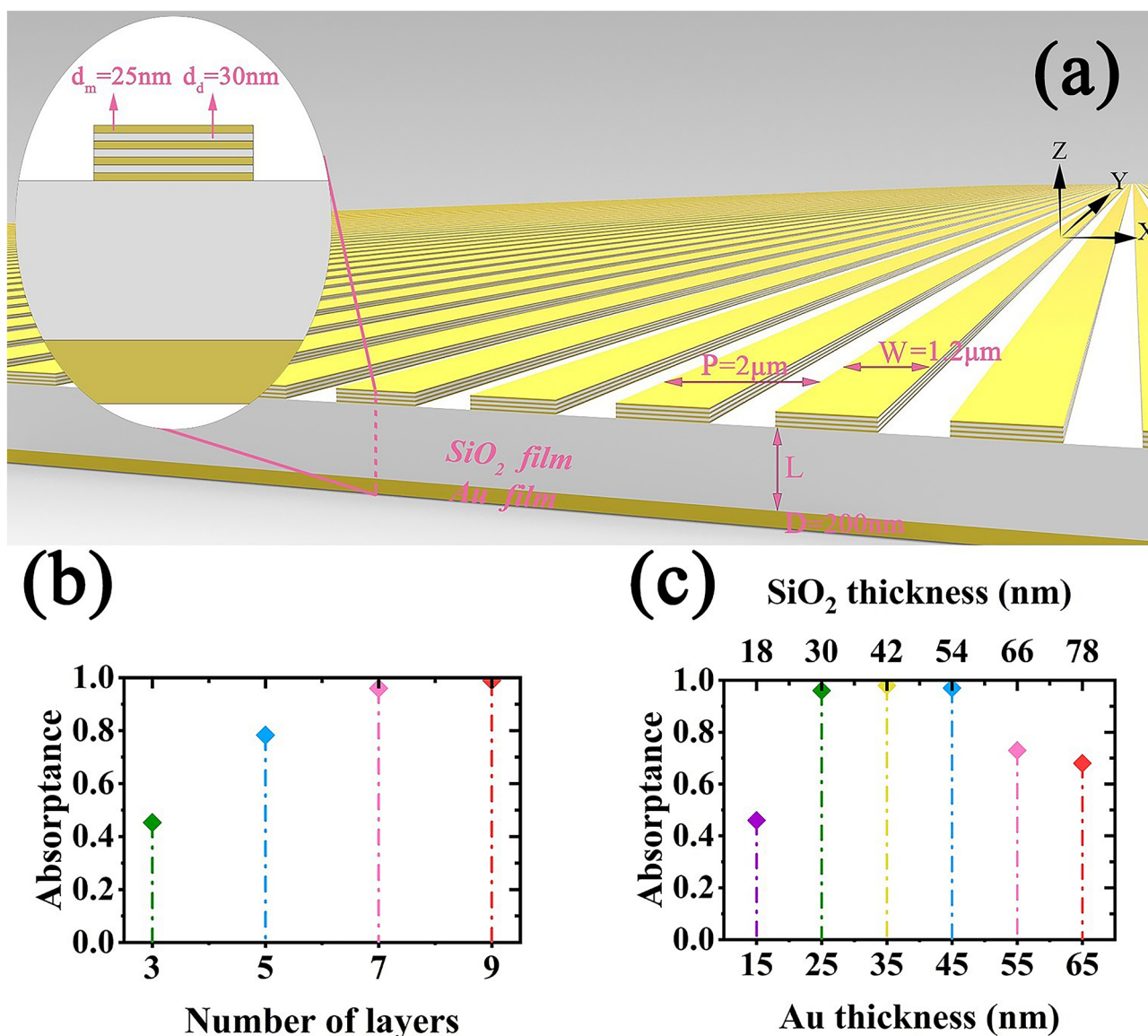


Fig. 1 a The schematic of the cavity-coupled perfect absorber structure, consisting of multilayer MIM nanowires deposited on a silicon substrate coated with a 200 nm thick layer of gold (Au) and a 1100 nm thick layer of silicon dioxide (SiO₂). b The dependence of simu-

lated absorbance on the layer number of multilayer MIM structure. c The dependence of simulated absorbance on the layer thickness of multilayer MIM structure

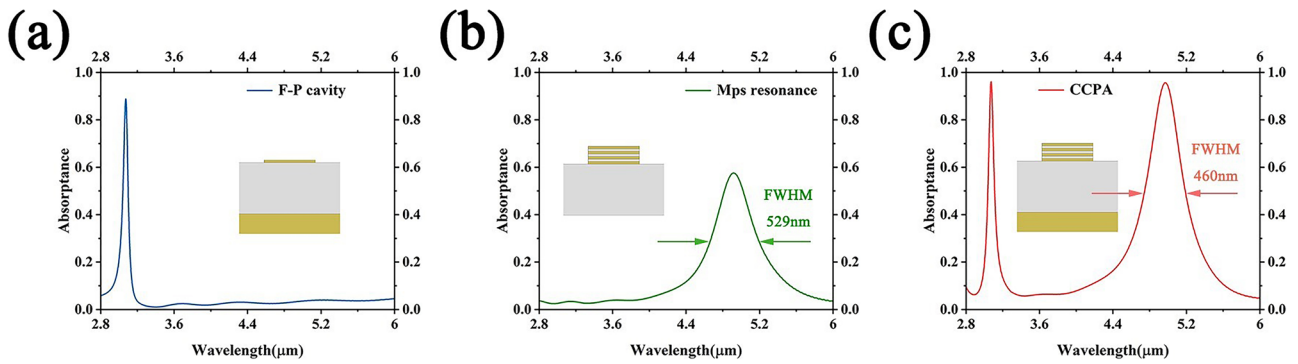


Fig. 2 **a** Absorbance of the F-P cavity mode. **b** Absorbance spectrum of the MPs resonance in the multilayer MIM structure. **c** Absorbance spectrum of the CCPA

(Au) layer, a silicon dioxide (SiO_2) layer, and a MIM grating composed of alternating layers of Au and SiO_2 deposited on a silicon wafer. In order to effectively analyze the optical response of the absorber, we use the commercial software Lumerical FDTD Solutions (2020 R2 version) to simulate the composite structure. The multilayer MIM structure plasmonic effect is unaffected if the length of the nanowires is much longer than that of the width of the nanowires. We reduce the three-dimensional (3-D) model to a 2-D one because both models will obtain similar results in simulations. Besides, the 2-D simulation model could save the time and computer resource compared to the 3-D one [28, 29]. The incident light source is set to TM-polarized light, and the magnetic field parallel to the Y axis sets the X axes in the simulation area as periodic boundary conditions. In order to eliminate echo interference, the Y axis is set to a perfect matching layer (PML). The reflectivity monitor is placed $8 \mu\text{m}$ above the structure. To ensure the convergence of the simulation structure,

we use a higher mesh accuracy (mesh accuracy = 6). Here, the absorbance (A) of the microstructure can be calculated by simulating the reflectance (R) and transmittance (T): $A = 1 - R - T$. The thicknesses of the nanowire width (W) and the period (P) of the multilayer MIM structure are set to 1200 nm and 2000 nm, respectively. The thickness of the metal mirror (D) is 200 nm, and the thickness of the SiO_2 dielectric layer (L) is tuned in the range of 0–3 μm . Figure 1b and c respectively showed the dependence of simulated absorbance on the layer numbers and layer thicknesses of the multilayer MIM structure. Simultaneously considering the absorption characteristics and the fabrication of the structure, 7-layer MIM grating is chose, and the thickness of Au layer and SiO_2 layer of the MIM grating is set to be 25 nm and 30 nm, respectively.

In order to demonstrate the absorption characteristics of each mode in the CCPA, we performed simulations of the absorption for each individual layer. Figure 2a, b, and c represents the absorption spectra for the individual F-P cavity

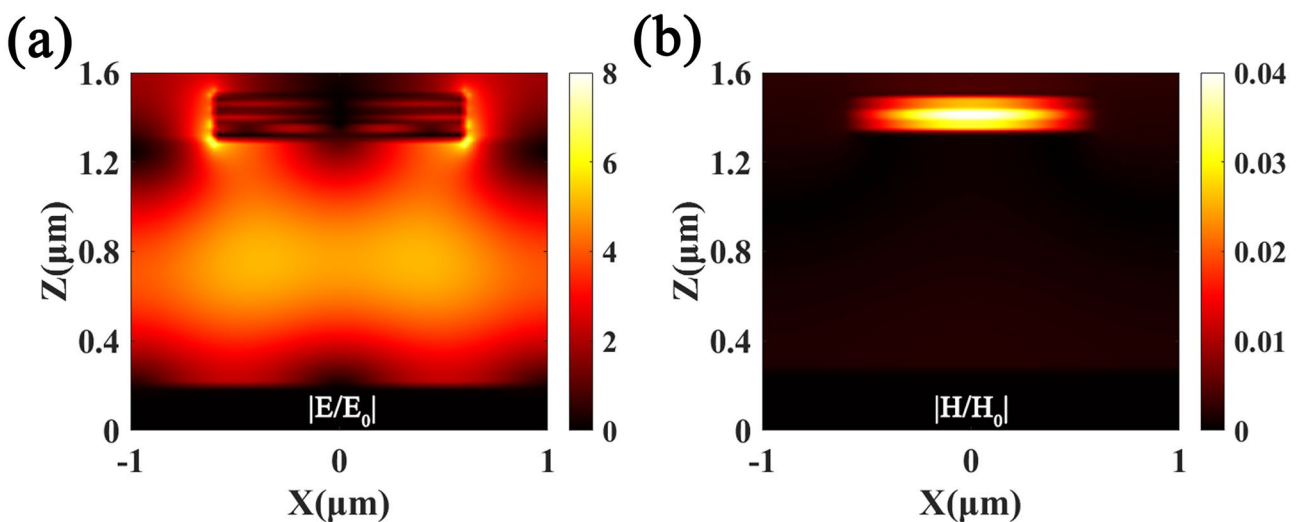


Fig. 3 **a** The electric field at the resonance wavelength of 3.1 μm . **b** The magnetic field at the resonance wavelength of 4.97 μm

mode, the individual MPs resonance mode in the multilayer MIM structure, and the CCPA, respectively. From the simulations, we can observe that, for the CCPA complex structure, two absorption peaks at 3.1 μm and 4.97 μm are obtained. Specially, the peak absorbance of the long-wave resonance is greatly enhanced compared to before coupling, increasing from 57 to 97%, which is close to perfect absorption, and the FWHM is reduced from 529 to 460 nm. The reasons for this phenomenon will be explained later.

To verify the physical origin of the two absorption peaks, we calculated the electric field and magnetic field distributions at the two resonant wavelengths. Figure 3a corresponds to the electric field at the resonance wavelength of 3.1 μm , where the energy is mainly localized in the underlying SiO₂ layer, indicating a typical Fabry-Pérot (F-P) cavity mode [30]. Figure 3b corresponds to the magnetic field at the resonance wavelength of 4.97 μm . The MIM structure can simply form a magnetic plasmon resonance that is well localized within the SiO₂ spacer [31].

Due to the regularity of the designed upper Au-SiO₂ multilayer MIM structure, we can mathematically describe it using MIM and F-P cavity theories. The general resonance conditions for this waveguide are defined as follows [32, 33]:

$$2W\beta + \varphi_r = 2m\pi \tag{1}$$

where β is the complex propagation constant, m is the resonance order, φ_r is the phase shift between the two surfaces of the waveguide, and W is the width of the grating stripe. So we can write the expression of m as follows:

$$m = (2W\beta + \varphi_r)/2\pi \tag{2}$$

it means we can figure out resonance order m only requiring the value of β . Fortunately, on the basis of waveguide theory,

the complex propagation constant β can be figured out by solving the following dispersion equations [32, 34]:

$$\begin{aligned} \varepsilon_d k_m + \varepsilon_m k_d \tan\left(\frac{k_d h}{2}\right) &= 0 \\ \beta^2 - \varepsilon_d k_0^2 &= k_d^2 \\ \beta^2 - \varepsilon_m k_0^2 &= k_m^2 \end{aligned} \tag{3}$$

where ε_d and ε_m are the dielectric constants of SiO₂ and Au, respectively. h is the thickness of the SiO₂ layer (30 nm and 1100 nm). $k_0 = 2\pi/\lambda$ is the free-space wave vector. Following the steps mentioned in Eqs. (1)–(3), we can obtain the values of β and confirm the resonance order m ($m = 1$). Additionally, in order to forecast the resonance wavelength λ_r by the mathematical model above, we introduce the concept of effective refractive index n_e of the MIM waveguide as $n_e = \beta/k_0$ [32]. According to it, we express the resonance wavelength λ_r as follows [35]:

$$\lambda_r = 2n_e W / (m - \varphi_r / 2\pi) \tag{4}$$

therefore, λ_r can be easily obtained as long as we substitute n_e and m into this equation. For a structure with the following parameters: $W = 1.2 \mu\text{m}$, $d_d = 30 \text{ nm}$, and $L = 1.1 \mu\text{m}$, the F-P cavity mode and the multilayer MIM structure resonant wavelengths obtained are at 3.106 μm and 4.9717 μm . The simulated resonant wavelengths were found to be 3.1 μm and 4.97 μm , indicating good agreement between the calculated one and that obtained by simulation. It is evident from the equations that the peak wavelength is directly proportional to the line width W , which also explains the redshift of the absorption peak with the increase of W in Fig. 4. The absorption peaks shift towards longer wavelengths when W increases from 0.8 to 1.2 μm . This redshift

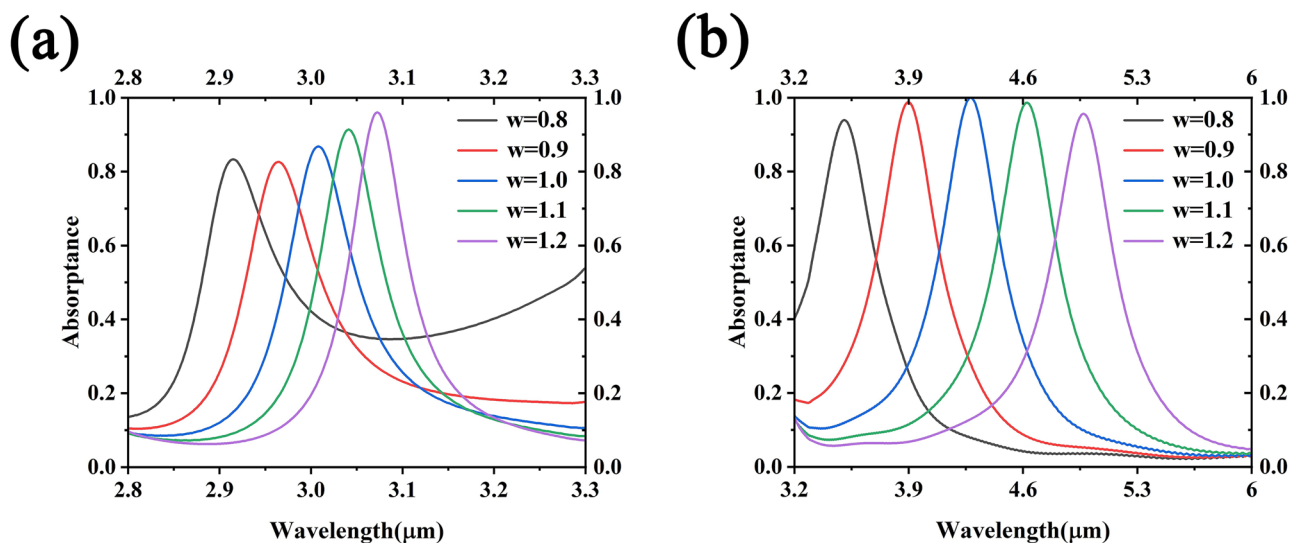


Fig. 4 a Dependence of F-P cavity resonance mode on W . b Dependence of multilayer MIM cavity resonance mode on W

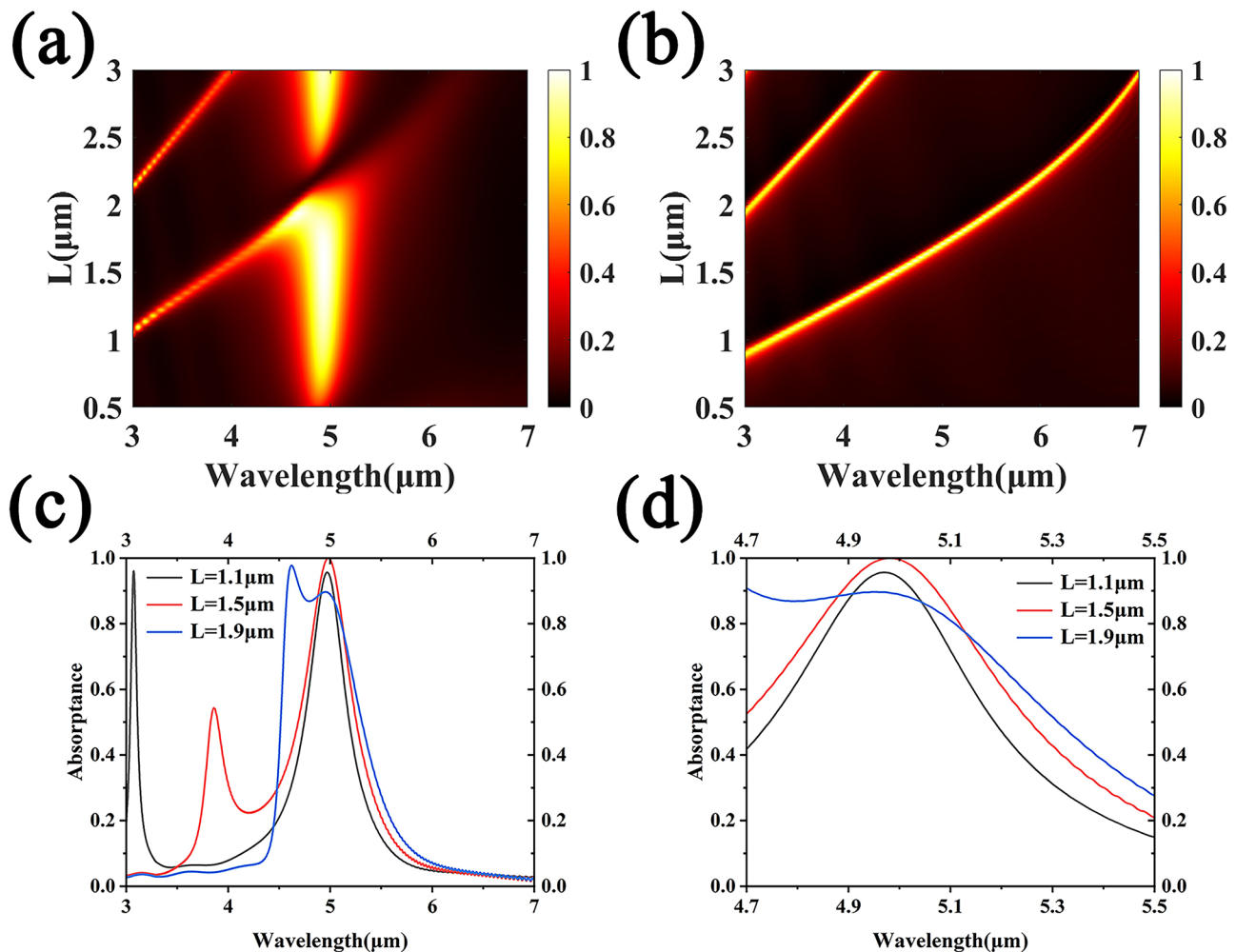


Fig. 5 **a** Parameter scan graph of L in the cavity-coupled perfect absorber. **b** Parameter scan graph of L in the F-P cavity. **c** The influence of different L on the absorption rate of the long-wavelength peak. **d** The amplified view of the long-wavelength absorption peak in Fig. 5c

behavior aligns with the general trend of grating-like microstructures [36, 37]. Based on this phenomenon, the tunability of the infrared resonant positions of the absorption peaks can be achieved, and the structure can maintain high absorption when W is varied within a certain range. The narrowband nature of this structure makes it suitable for detecting the absorption characteristics of target gases, and it can be used as a compact and selective thermal light source for gas sensing. At thermal equilibrium, the emissivity of a material is equal to its absorptance (Kirchhoff's law of thermal radiation), which means that the supersurface radiates energy in the same narrowband spectral range. Common harmful gases have characteristic spectral features in the mid-infrared region, such as CH₄ (3.61 μm), NO (5.1 μm), NO₂ (6.3 μm), CO (4.46 μm), and CO₂ (4.45 μm). The designed metasurface in this study has a mid-infrared emission peak that matches the characteristic spectra of the mentioned harmful gases [38].

To explore the relationship between these two modes, the simulated absorption is plotted as a function of L and the incident wavelength in Fig. 5. The thickness of the reflective mirror Au layer is set to 200 nm, resulting in complete suppression of transmitted light. The absorptance (A) was calculated through the reflectance (R) and transmittance (T) obtained by simulation: $A = 1 - R - T$. In Fig. 5a, two types of modes can be observed, where we define the mode that undergoes redshift as mode A, and the mode with a constant resonance position as mode B. For mode A, the resonance shifts to longer wavelengths as the thickness of the SiO₂ layer L increases. This behavior is a clear indication of the F-P cavity mode formed between the reflective mirror and the bottom metal layer of the multilayer MIM structure. Moreover, as the cavity length increases, higher-order modes emerge. For mode B, regardless of the SiO₂ layer thickness L variation, the resonance wavelength remains almost constant. When mode A's redshift nearly coincides with mode B's resonance peak

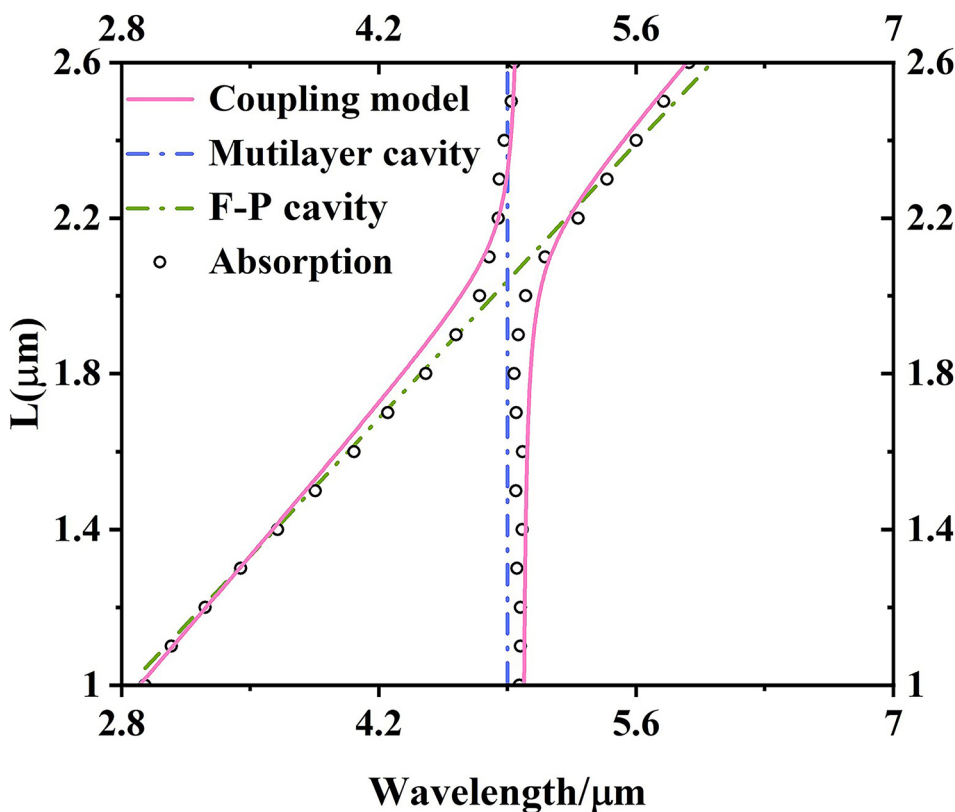
position, the resonance position exhibits an anticross effect. Figure 5b shows the parameter scanning of the spectrum of the individual F-P cavity where the multilayer MIM is replaced with a single-layer metal nanowire during simulation. By comparing Fig. 5a and b, it is worth noting that each order of the F-P mode undergoes a blueshift. And an anticross-coupling phenomenon is observed due to the overlap of resonance positions in Fig. 5a, causing the light waves to not enter mode B’s channel. This results in the multilayer MIM structure being in a low absorption state, indicating that the absorption state has two distinct states of “on” and “off.” Therefore, by controlling the thickness of the SiO₂ layer, it is possible to achieve the switching between the absorption states at 4.97 μm, which exhibits excellent optical characteristics suitable for optical switches in optical computing [39]. This greatly enhances its application potential. From Fig. 5c and d, it is evident that the two modes are not isolated from each other. When the two modes interact, the value of L can be changed to adjust the absorptance of the long-wave absorption peak. In other words, this interaction can vary according to the tuning means, and the coupling between the two absorption modes leads to the ability to control the constructive interaction of absorption [40, 41]. The enhancement effect of different F-P cavities with different cavity lengths on the multilayer MIM structure varies based on their parameters. When L is equal to 1.5 μm, the absorptance can be tuned to 100%.

To explain the interaction observed above, the interaction between the first-order Fabry–Perot (F-P) cavity and the MPs resonance mode in multilayer MIM structure can be understood as a 2 × 2 Hamiltonian matrix. This model describes the coupling behavior of the original “bare” modes in the system, and the Hamiltonian matrix is represented as follows [42, 43]:

$$H = \begin{pmatrix} E_1 & V \\ V & E_2 \end{pmatrix} \tag{5}$$

E1 and E2 represent the energies of the F-P cavity mode and the MPs resonance mode in multilayer MIM structure, respectively. V is the coupling coefficient. After introducing V, the eigenvalues of the Hamiltonian represent the new eigenfrequencies of the coupled system. So by solving the eigenvalues of the Hamiltonian matrix, the resonance position of two coupled modes can be predicted. Firstly, we extracted the unperturbed energy of the first-order F-P cavity mode from Fig. 5b, and the resonance position of the MPs resonance mode in multilayer MIM structure is at 4.97 μm. In Fig. 6, the unperturbed first-order F-P cavity mode and MPs resonance mode in multilayer MIM structure are depicted by the green and blue dashed lines, respectively. To achieve good consistency, V is chosen as 8 meV. The resonance positions predicted by the coupled system are

Fig. 6 The dependence of the resonance positions on L using the coupled model. The open circles represent the calculated positions of the absorption peaks. The pink solid line represents the predicted resonance positions obtained through the coupled model. The blue and green dashed lines depict the positions of the unperturbed F-P cavity and multilayer MIM cavity modes, respectively



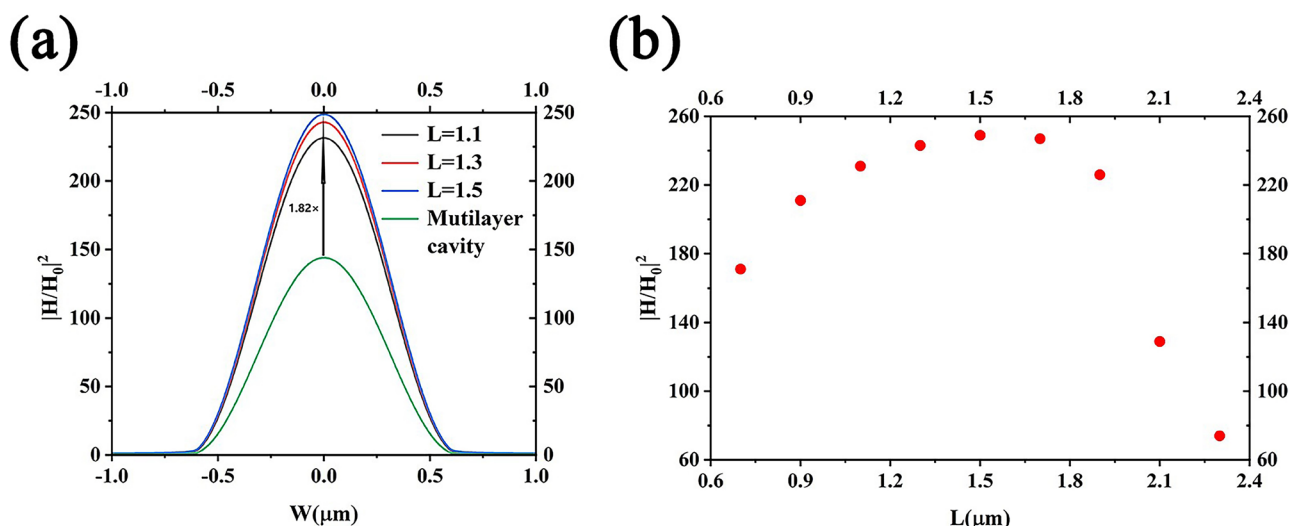
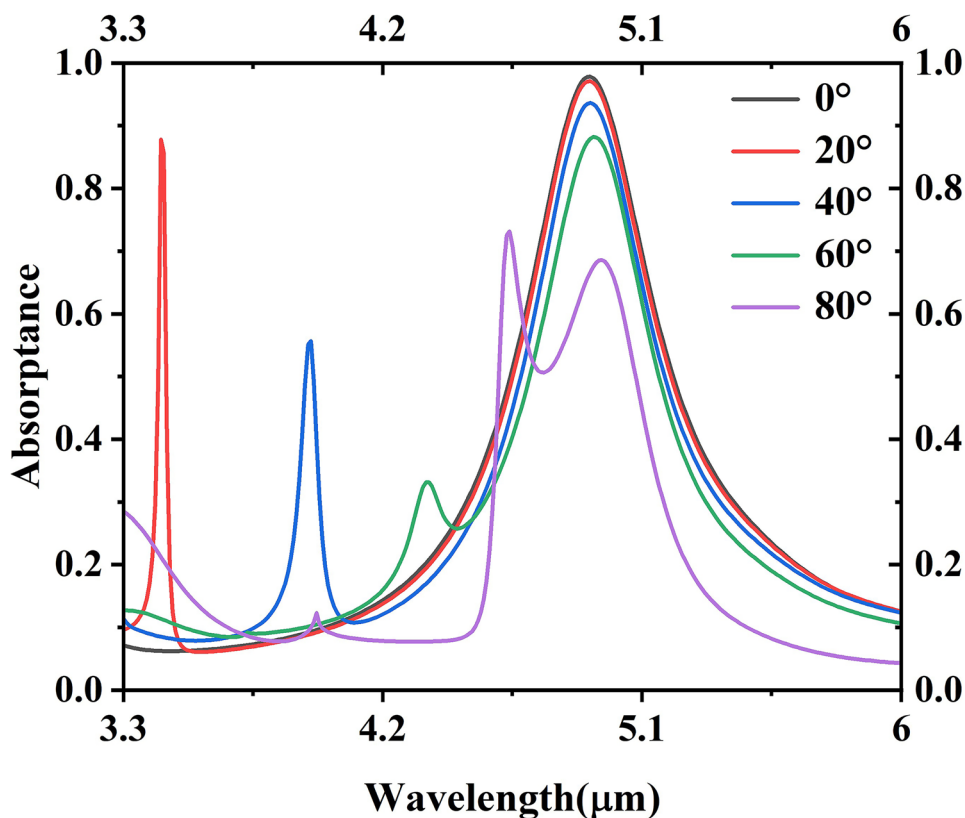


Fig. 7 **a** The magnetic field distribution within the multilayer MIM structure normalized to the incident light. **b** The relative magnetic field intensity in multilayer MIM structure under different F-P cavity lengths

shown as the pink solid line in the graph, whereas the open circles represent the positions of resonances of the coupled system extracted from Fig. 5a. Clearly, the resonance peak positions predicted by the coupled system are in excellent agreement with the computed resonance peak positions in the absorption spectrum, exhibiting significant anticrossing phenomena at the intersections of these lines.

To explain the occurrence of the anticrossing phenomenon, we simulated the magnetic field near the coupling region, as shown in Fig. 7a. The magnetic field distribution within the cavity has been normalized to the incident light magnetic field. It can be observed that when the two modes are coupled, the magnetic field in the multilayer MIM structure is significantly enhanced. The enhancement factor obtained is

Fig. 8 The absorbance of the absorber at different incident angles



greater than 1.8 compared to the enhancement factor on the semi-infinite SiO_2 substrate. Moreover, the enhancement factor increases as we approach the coupling position, indicating that the multilayer MIM structure enhances the local field capability of light. This is the reason for the occurrence of the perfect absorption peak when establishing the coupling structure in the beginning of this study. Such near-field enhancement is also crucial in sensing applications. Figure 7b shows the relative magnetic field intensity in multilayer MIM structure under different F-P cavity lengths. We can see that when L is equal to $1.5 \mu\text{m}$, the relative magnetic field intensity is the highest, which is 250 times that of the incident optical magnetic field. This explains why the absorptivity in Fig. 5c is 100% when L is equal to $1.5 \mu\text{m}$.

The stability of the structure at different incident angles is also considered as shown in Fig. 8. The results indicate that for TM-polarized light at incident angles ranging from 0 to 60° , the long-wavelength absorption peak remains

unchanged, while the short-wavelength absorption peak experiences some redshift. Therefore, for the long-wavelength perfect absorption peak, the performance of the designed structure remains efficient and stable at different incident angles, exhibiting an “omnidirectional” characteristic when the incident angle of light ranges from 0 to 60° . This is advantageous for dual applications in gas sensing and mid-infrared perfect absorber devices.

Experimental Section

The fabrication of metal-dielectric hybrid structures has been demonstrated using a combination of UV lithography and magnetron sputtering coating process, as shown in Fig. 9a. Firstly, 200 nm of Au and 900 nm of SiO_2 were sputtered on a Si substrate (step 1). Next, a layer of photoresist ($\approx 500 \text{ nm}$) was spun-coated onto the SiO_2

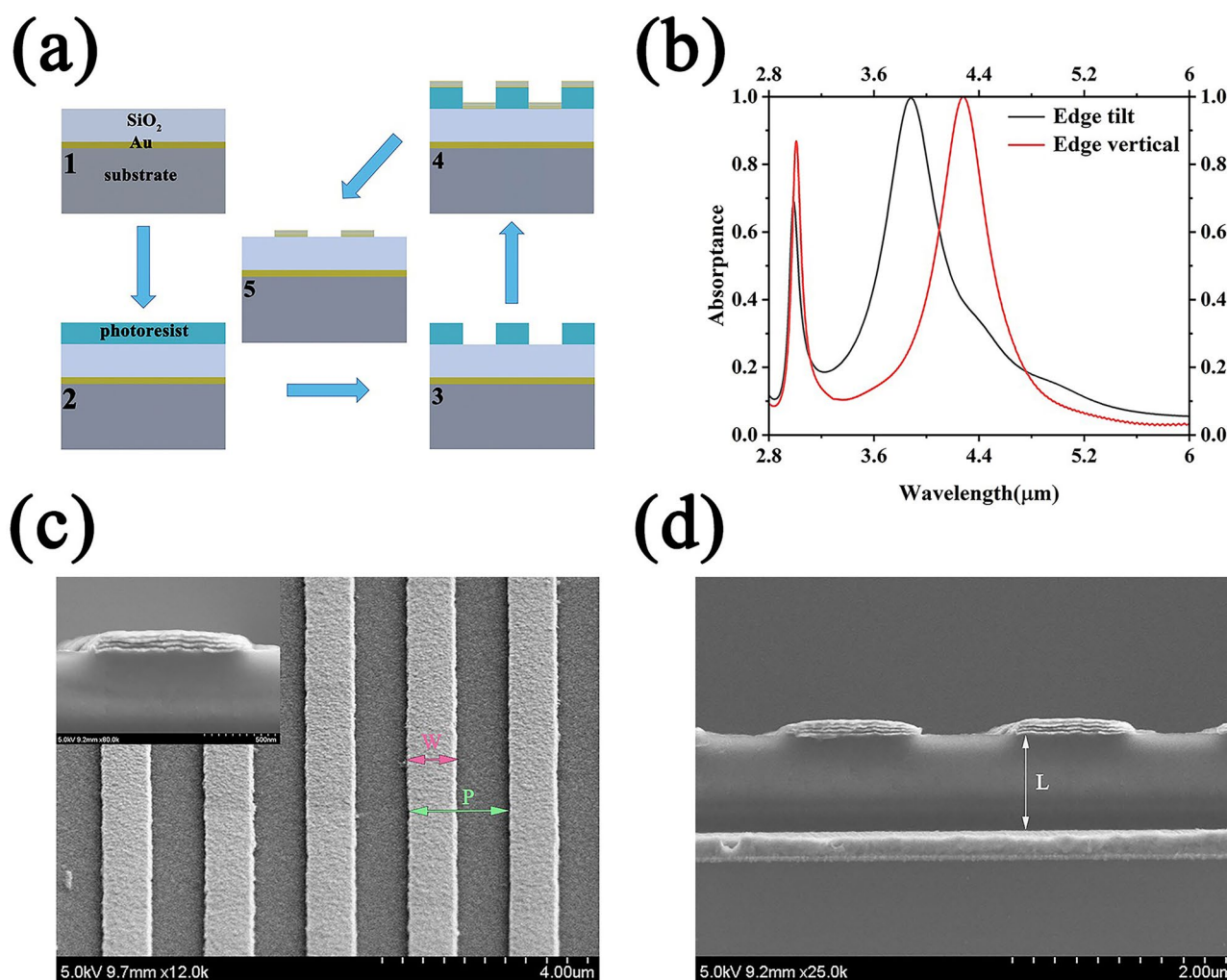
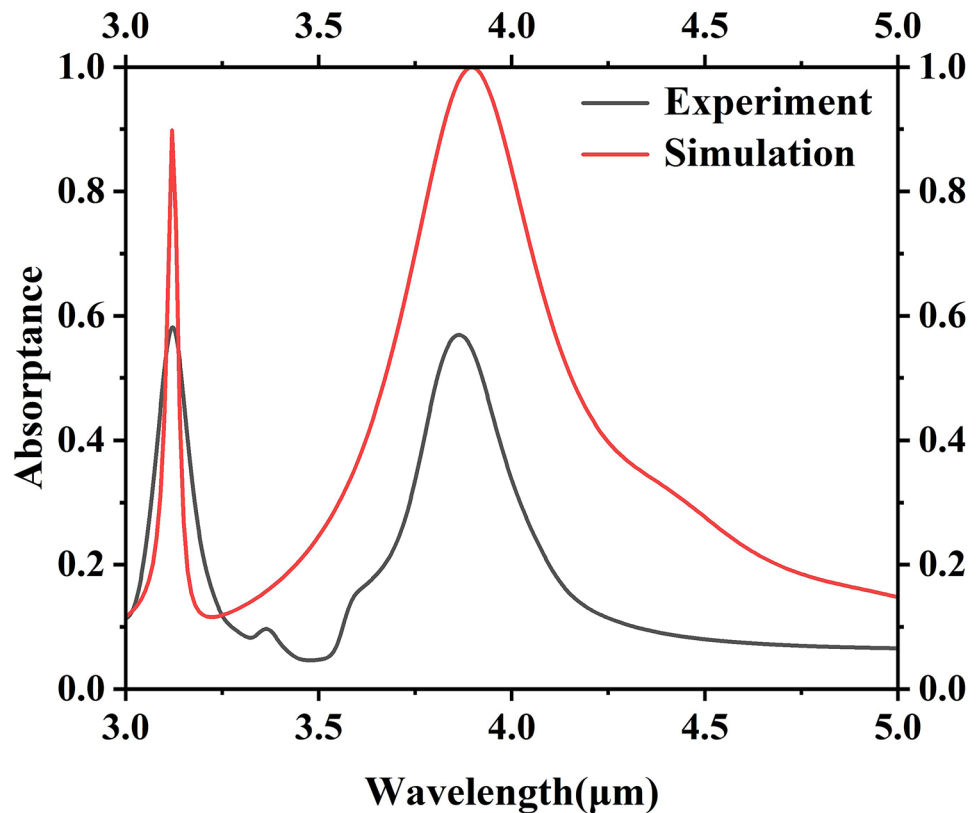


Fig. 9 a Schematic illustration of the fabrication method based on EBL, lift-off process, and consecutive steps of dielectric and metal deposition. b The absorbance of the structure edge tilt. c The top view of the microstructure. d The cross-sectional view of the microstructure

Fig. 10 The mid-infrared absorbance measured by FTIR (Fourier transform infrared) spectroscopy



substrate (step 2), and a series of periodic 2 μm wide and 1 μm tall lines were patterned using UV lithography (step 3). Then, a 10-nm thick Cr layer was deposited using magnetron sputtering in these lines as a connecting layer to prevent delamination, followed by the sputtering of 7 alternating layers of Au and SiO_2 (step 4). Finally, the photoresist was removed by ultrasonic cleaning in acetone (step 5). During the photoresist stripping step, the metal-dielectric film on the sidewall detached, resulting in trapezoidal lines with tilted edges. This led to a deviation in the resonance peak position from the previous simulations for rectangular lines with perpendicular edges. As shown in Fig. 9b, a phenomenon of resonance peak blue shift (tilted at 45°) and increased linewidth was observed. However, the underlying physical mechanism of excitation remained the same, confirming the correctness of the design of the hybrid structure. Figure 9b and c shows the scanning electron microscope images of the microstructures from a top view and cross-section, respectively, indicating the successful fabrication of the samples with good quality.

Fig. 10 shows the absorption spectra of the composite structure experimentally measured using a Fourier-transform infrared spectrometer (FTIR) with polarized incident light. The wavelength range of the system is from 400 to 16.7 μm , and a polarizer was used to characterize the polarized light. The reflection accessory was set at an angle of 12° to simulate the 12° inclined incident

absorption spectra of the edge-tilted structure (shown as the red solid line in Fig. 10), which indicates that the absorption peaks do not shift significantly compared to the vertical incident case shown in Fig. 9b. The experimentally fabricated samples have successfully excited the designed resonance peaks (shown as the black solid line in Fig. 10). The flatness of the film layer in the preparation of gratings affects the absorption characteristics of the structure, resulting the actual absorbance decreases compared to the simulation results. The resonance peak position in the experiment corresponds well with the simulation, verifying the correctness of the simulation.

Conclusion

In summary, we propose a composite structure based on the mode coupling of the F-P cavity and multilayer MIM structure and optimize the parameters to enhance the absorption. In the mid-wavelength infrared (MWIR) atmospheric window (3–5 μm), the structure exhibits tunable dual-peak narrowband absorption, with the long-wavelength absorption peak achieving perfect absorption and the short-wavelength absorption peak reaching up to 95% absorption. The resonance wavelength and absorbance in the multilayer MIM cavity can be controlled by adjusting the width of the lines and the thickness of the SiO_2 layer. The resonance

wavelengths were calculated using F-P and MIM theory and experimentally validated, showing relatively agreement with the values obtained from FDTD simulations, thus verifying the accuracy of our design. This novel structure introduces a new approach to realizing mid-infrared absorbers with both perfect absorption and tunable characteristics, making it suitable for infrared radiation heat sources that match the characteristic spectra of common harmful gases.

Author contribution Writing, Zhihui Wei and Hai Liu; visualization, Jian Zhang, Bo Wang, Haolong Tang, Qiang Li, Kai Wang; revision, Zhenfeng Shen, Haigui Yang, Dongzhi Shan, Yuanhang Zhao, Yi Zhao, Xiaoyi Wang. All authors have read and agreed to the published version of the manuscript.

Funding This work was supported by the National Natural Science Foundation of China (Nos. 12204478).

Availability of Data and Materials All data included in this article are available from the corresponding author upon reasonable request.

Code Availability All codes included in this article are available from the corresponding author upon reasonable request.

Declarations

Ethics Approval Not applicable.

Consent to Participate Not applicable.

Consent for Publication Not applicable.

Competing Interests The authors declare no competing interests.

References

- Ma X-C, Dai Y, Yu L, Huang B-B (2016) Energy transfer in plasmonic photocatalytic composites. *Light Sci Appl* 5:e16017. <https://doi.org/10.1038/lsa.2016.17>
- Smith DR, Padilla WJ, Vier DC, Nemat-Nasser SC, Schultz S (2000) Composite medium with simultaneously negative permeability and permittivity. *Phys Rev Lett* 84:4184–4187. <https://doi.org/10.1103/PhysRevLett.84.4184>
- Shelby RA, Smith DR, Schultz S (2001) Experimental verification of a negative index of refraction. *Science* 292:77–79. <https://doi.org/10.1126/science.1058847>
- Yu N, Aieta F, Genevet P, Kats MA, Gaburro Z, Capasso F (2012) A broadband, background-free quarter-wave plate based on plasmonic metasurfaces. *Nano Lett* 12:6328–6333. <https://doi.org/10.1021/nl303445u>
- Huang X, Lai Y, Hang ZH, Zheng H, Chan CT (2011) Dirac cones induced by accidental degeneracy in photonic crystals and zero-refractive-index materials. *Nat Mater* 10:582–586. <https://doi.org/10.1038/nmat3030>
- Khorasaninejad M, Chen WT, Devlin RC, Oh J, Zhu AY, Capasso F (2016) Metalenses at visible wavelengths: diffraction-limited focusing and subwavelength resolution imaging. *Science* 352:1190–1194. <https://doi.org/10.1126/science.aaf6644>
- Lin H, Xu ZQ, Cao G, Zhang Y, Zhou J, Wang Z, Wan Z, Liu Z, Loh KP, Qiu CW, Bao Q, Jia B (2020) Diffraction-limited imaging with monolayer 2D material-based ultrathin flat lenses. *Light Sci Appl* 9:137. <https://doi.org/10.1038/s41377-020-00374-9>
- Ni X, Wong ZJ, Mrejen M, Wang Y, Zhang X (2015) An ultrathin invisibility skin cloak for visible light. *Science* 349:1310–1314. <https://doi.org/10.1126/science.aac9411>
- Fang N, Lee H, Sun C, Zhang X (2005) Sub-diffraction-limited optical imaging with a silver superlens. *Science* 308:534–537. <https://doi.org/10.1126/science.1108759>
- Mann SA, Garnett EC (2015) Resonant nanophotonic spectrum splitting for ultrathin multijunction solar cells. *ACS Photonics* 2:816–821. <https://doi.org/10.1021/acsp Photonics.5b00260>
- Park B, Yun SH, Cho CY, Kim YC, Shin JC, Jeon HG, Huh YH, Hwang I, Baik KY, Lee YI, Uhm HS, Cho GS, Choi EH (2014) Surface plasmon excitation in semitransparent inverted polymer photovoltaic devices and their applications as label-free optical sensors. *Light Sci Appl* 30:e222. <https://doi.org/10.1038/lsa.2014.103>
- Cetin AE, Etezadi D, Galarreta BC, Busson MP, Eksioğlu Y, Altug H (2015) Plasmonic nanohole arrays on robust hybrid substrate for highly sensitive label-free biosensing. *ACS Photonics* 2:1167. <https://doi.org/10.1021/acsp Photonics.5b00242>
- Qu Y, Li Q, Gong H, Du K, Bai S, Zhao D, Ye H, Qiu M (2016) Spatially and spectrally resolved narrowband optical absorber based on 2D grating nanostructures on metallic films. *Adv Optical Mater* 4:480. <https://doi.org/10.1002/adom.201500651>
- Cao T, Wei C, Simpson RE, Zhang L, Cryan MJ (2015) Broadband polarization-independent perfect absorber using a phase-change metamaterial at visible frequencies. *Sci Rep* 4:3955. <https://doi.org/10.1038/srep03955>
- Liu K, Zeng X, Jiang S, Ji D, Song H, Zhang N, Gan Q (2014) A large-scale lithography-free metasurface with spectrally tunable super absorption. *Nanoscale* 6:5599. <https://doi.org/10.1039/c4nr00747f>
- Xuan Y (2014) An overview of micro/nanoscaled thermal radiation and its applications. *Photonics Nanostruct Fundam Appl* 12:93. <https://doi.org/10.1016/j.photonics.2014.02.003>
- Li W, Valentine J (2014) Metamaterial perfect absorber based hot electron photodetection. *Nano Lett* 14:3510–3514. <https://doi.org/10.1021/nl501090w>
- Chen M, Chau Y, Tsai D (2008) Three-dimensional analysis of scattering field interactions and surface plasmon resonance in coupled silver nanospheres. *Plasmonics* 3:157–164. <https://doi.org/10.1007/s11468-008-9069-8>
- Chau Y, Yeh H, Tsai D (2010) A new type of optical antenna: plasmonics nanoshell bowtie antenna with dielectric hole. *Journal of Electromagnetic Waves and Applications* 24:1621–1632. <https://doi.org/10.1163/156939310792149588>
- Chou Chau Y, Syu J, Chao C, Chiang H, Lim C (2017) Design of crossing metallic metasurface arrays based on high sensitivity of gap enhancement and transmittance shift for plasmonic sensing applications. *J Phys D Appl Phys* 50:045105. <https://doi.org/10.1088/1361-6463/aa506b>
- Wu Y, Xie P, Ding Q, Li Y, Yue L, Zhang H, Wang W (2023) Magnetic plasmons in plasmonic nanostructures: an overview. *J Appl Phys* 133:030902. <https://doi.org/10.1063/5.0131903>
- Tittl A, Michel AK, Schäferling M, Yin X, Gholipour B, Cui L, Wuttig M, Taubner T, Neubrech F, Giessen H (2015) A switchable mid-infrared plasmonic perfect absorber with multispectral thermal imaging capability. *Adv Mater* 27:4597–4603. <https://doi.org/10.1002/adma.201502023>
- Liu X, Gao J, Yang H, Wang X, Guo C (2018) Multiple infrared bands absorber based on multilayer gratings. *Opt Commun* 410:438–442. <https://doi.org/10.1016/j.optcom.2017.10.046>
- Chou Chao C, Chou Chau Y, Chiang H (2020) Highly sensitive metal-insulator-metal plasmonic refractive index sensor with a centrally coupled nanoring containing defects. *J Phys D Appl Phys* 54:115301. <https://doi.org/10.1088/1361-6463/abc7f>

25. Chou Chau Y (2021) Multiple-mode bowtie cavities for refractive index and glucose sensors working in visible and near-infrared wavelength ranges. *Plasmonics* 16:1633–1644. <https://doi.org/10.1007/s11468-021-01431-8>
26. Chou Chau Y, Ming T, Chou Chao C, Thotagamuge R, Kooh M, Huang H, Lim C, Chiang H (2021) Significantly enhanced coupling effect and gap plasmon resonance in a MIM-cavity based sensing structure. *Sci Rep* 11:18515. <https://doi.org/10.1038/s41598-021-98001-z>
27. Chanda D, Shigeta K, Truong T, Lui E, Mihi A, Schulmerich M, Braun PV, Bhargava R, Rogers JA (2011) Coupling of plasmonic and optical cavity modes in quasi-three-dimensional plasmonic crystals. *Nat Commun* 2:479. <https://doi.org/10.1038/ncomms1487>
28. Chou Chao Y, Chou Chao C, Huang H, Wang Y, Chiang H, Idris M, Masri Z, Lim C (2019) Strong and tunable plasmonic field coupling and enhancement generating from the protruded metal nanorods and dielectric cores. *Results Phys* 13:102290. <https://doi.org/10.1016/j.rinp.2019.102290>
29. Jumat S, Chou Chao C, Chou Chau Y, Mahadi A, Kooh M, Thotagamuge R, Chiang H (2021) Plasmonic refractive index sensor based on the combination of rectangular and circular resonators including baffles. *Chin J Phys* 71:286–299. <https://doi.org/10.1016/j.cjph.2021.02.006>
30. Ameling R, Langguth L, Hentschel M, Mesch M, Braun P, Giessen H (2010) Cavity-enhanced localized plasmon resonance sensing. *Appl Phys Lett* 97:253116. <https://doi.org/10.1063/1.3530795>
31. Zhang C, Fang J, Yang W, Song Q, Xiao S (2017) Enhancing the magnetic resonance via strong coupling in optical metamaterials advanced optical materials 5:1700469. <https://doi.org/10.1002/adom.201700469>
32. Hu F, Yi H, Zhou Z (2011) Band-pass plasmonic slot filter with band selection and spectrally splitting capabilities. *Opt Express* 19:4848–4855. <https://doi.org/10.1364/OE.19.004848>
33. Mihail B, Elaine M, Dietrich A, Jerald A, Cindy C, Allan S, Keiko M, Hoang T, Tiziana C (2013) Plasmonic black metals in resonant nanocavities. *Appl Phys Lett* 102:251105. <https://doi.org/10.1063/1.4802910>
34. Petschulat J, Helgert C, Steinert M, Bergner N, Rockstuhl C, Lederer F, Pertsch T, Tünnermann A, Kley EB (2010) Plasmonic modes of extreme subwavelength nanocavities. *Opt Lett* 35:2693–2695. <https://doi.org/10.1364/OL.35.002693>
35. Liu X, Gao J, Yang H, Wang X (2016) Si-based near-infrared narrowband absorber based on square Au patches. *J Opt Soc Am B* 33:2149–2153. <https://doi.org/10.1364/JOSAB.33.002149>
36. Sobhani A, Knight MW, Wang Y, Zheng B, King NS, Brown LV, Fang Z, Nordlander P, Halas NJ (2013) Narrowband photodetection in the near-infrared with a plasmon-induced hot electron device. *Nat Commun* 4:1643. <https://doi.org/10.1038/ncomms2642>
37. Knight MW, Wang Y, Urban AS, Sobhani A, Zheng BY, Nordlander P, Halas NJ (2013) Embedding plasmonic nanostructure diodes enhances hot electron emission. *Nano Lett* 13:1687–1692. <https://doi.org/10.1021/nl400196z>
38. Mihai L, Mihalcea R, Tomescu R, Paun C, Cristea D (2022) Selective mid-IR metamaterial-based gas sensor system: proof of concept and performances tests. *Nanomaterials (Basel)* 12:1009. <https://doi.org/10.3390/nano12061009>
39. Koch U, Hoessbacher C, Emboras A, Leuthold J (2017) Optical memristive switches. *J Electroceram* 39:239–250. <https://doi.org/10.1007/s10832-017-0072-3>
40. Sabaruddin N, Tan Y, Chou Chao C, Kooh M, Chou Chau Y (2023) High sensitivity of metasurface-based five-band terahertz absorber. *Plasmonics* 1:1–13. <https://doi.org/10.1007/s11468-023-01989-5>
41. Chou Chao C, Chen S, Huang H, Chou Chau Y (2023) Near- and mid-infrared quintuple-band plasmonic metamaterial absorber. *Plasmonics* 18:1581–1591. <https://doi.org/10.1007/s11468-023-01881-2>
42. Christ A, Tikhodeev SG, Gippius NA, Kuhl J, Giessen H (2003) Waveguide-plasmon polaritons: strong coupling of photonic and electronic resonances in a metallic photonic crystal slab. *Phys Rev Lett* 91:183901. <https://doi.org/10.1103/PhysRevLett.91.183901>
43. Zentgraf T, Zhang S, Oulton RF, Zhang X (2009) Ultranarrow coupling-induced transparency bands in hybrid plasmonic systems. *Phys Rev B* 80:195415. <https://doi.org/10.1103/physrevb.80.195415>

Publisher's Note Springer Nature remains neutral with regard to jurisdictional claims in published maps and institutional affiliations.

Springer Nature or its licensor (e.g. a society or other partner) holds exclusive rights to this article under a publishing agreement with the author(s) or other rightsholder(s); author self-archiving of the accepted manuscript version of this article is solely governed by the terms of such publishing agreement and applicable law.